# Matter-Wave Index of Refraction, Inertial Sensing, and Quantum Decoherence in an Atom Interferometer

Troy D. Hammond[1]*, Michael S. Chapman[1], Alan Lenef[1], Jörg Schmiedmayer[1,2], Edward T. Smith[1], Richard A. Rubenstein[1], David A. Kokorowski[1], and David E. Pritchard[1]

[1] *Department of Physics and Research Laboratory of Electronics, Massachusetts Institute of Technology, Cambridge, MA 02139, USA*

[2] *Institut für Experimentalphysik, Universität Innsbruck, A-6020 Innsbruck, Austria*

Received January 26, 1997

We review three recent experiments showing the application of atom interferometers in a variety of areas. We present initial results for the dispersion of the index of refraction for matter-waves. This experiment determines the phase shift in atom-atom scattering where it establishes the existence of glory oscillations in this quantity. The fundamental issue of decoherence in quantum mechanics was probed in a second experiment, a version of Feynman's *gedanken* experiment in which a single photon was scattered from each atom as it passed through the interferometer. The "which path" information that could in principal be gained by observing the scattered photon is shown to cause a loss of contrast in the atom interference fringes. We show that the lost coherence can be regained by observing interference fringes formed only by those atoms which scatter a photon into a small subset of possible final directions. In the third experiment, we demonstrate the high sensitivity of atom interferometers to inertial effects, showing that our interferometer can measure small rotations with a sensitivity of better than 50 milli-earthrate (0.1 deg per minute) in a one second measurement.

## I. Introduction

Since its origins in 1991, atom interferometry has already demonstrated powerful impact in three major areas of application: studies of atomic and molecular properties, fundamental studies, and inertial measurements. In this paper we discuss a recent application of our atom interferometer in each of these three areas. We present the first experimental measurement of the velocity dependence of the phase shift in atomic collisions, showing a new type of "glory oscillation." Second, we address the fundamental issue of the amount of loss of atomic coherence when a single photon is scattered from an atom passing through an interferometer. We will also demonstrate a method of recovery for this "lost" coherence. Finally, we discuss a recent inertial study: a precise measurement of absolute rotation rate, demonstrating reproducibility at the level of 50 milli-earthrates per $\sqrt{\text{sec}}$, performance typical of commercial laser gyros. Details of the apparatus and setup for each of these experiments are reviewed in Ref [1]. Data on velocity dependence are found in Ref [2].

## II. Velocity dependent index of refraction

With the goal of contributing a fundamentally new tool for studying atomic collisions, our group performed the first measurements of the phase shift of an atom due to a collision with another atom using our atom interferometer[3]. Since this initial publication, several theory papers[4–7] have discussed the unique sensitivity of this new tool, with an emerging consensus that direct

*Present address: McKinsey & Co., 301 Grant Street, Suite 2600, Pittsburgh PA 15219; troy@amo.mit.edu

phase shift measurements are in general very sensitive to the long range part of the relevant interatomic potentials. In this section we describe theory and recent experimental measurements of the dependence of this phase shift on center of mass energy, accomplished by varying the sodium beam velocity in our atom interferometer (Fig. (1)). These data promise to provide new information to help accurately determine the shape of the interatomic potential.

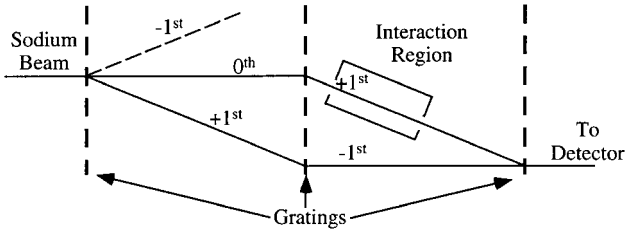


Figure 1. Schematic of the M.I.T. atom interferometer. (Not to scale.) The beam propogates from left to right and only the diffracted orders that contribute to the interference are shown. The interaction located near the second grating where the beams are most separated.

## II.1. Theory

### II.1.1. Index of refraction

A matter-wave experiences absorption and a phase shift as it passes through a gas just as light does when it passes through the atmosphere. For example, if a wave described by $\Psi = e^{ik_0 x}$X, which has the free space wavevector $k_0$, enters a uniform refractive medium at $x = 0$, at some later point $x = L$ we can phenomenologically expect the (forward traveling) wavefunction to have the form

$$\Psi = e^{ik_0 L} e^{i\phi NL} e^{-\sigma NL}. \qquad (1)$$

Both $\phi$ and $\sigma$ are to be interpreted as cross sections. That is, when multiplied by the number density $N$ of scattering particles and the length of propagation $L$, they determine respectively the additional phase shift $\phi NL$ and the attenuation, given by $|\Psi|^2$. (The relation between $\sigma$ and the total scattering cross section is $\sigma_T = 2\sigma$.)

This phase shift and decay of amplitude can be fully described by introducing a new wavevector $k = nk_0$, where $n$ is the complex index of refraction that is valid inside the medium. Equating $\Psi$ from Eq. (1) to $e^{ink_0 x}$ we find

$$n = 1 + \frac{\phi NLk + i\sigma NL}{k_0 L} = 1 + \frac{N}{k_0}(\phi + i\sigma) \ . \qquad (2)$$

We see that the complex quantity $n-1$ now contains the necessary information to express both the phase shift and amplitude decay, and it is linear in the number density $N$.

The index of refraction $n$, which describes the passage of a wave through a medium on the macroscopic scale, is determined on the microscopic (quantum mechanical) scale by a parameter called the scattering amplitude $f(\vec{k}', \vec{k})$. Here, $\vec{k}$ is the incoming wavevector and $\vec{k}'$ is the outgoing wavevector with $|k'| = |k|$ for elastic scattering. Because of the equality $|k'| = |k|6$, we unambiguously write $f(\vec{k}', \vec{k})$ as $f(k, \theta)$, where $\theta$ is the angle between $\vec{k}'$ and $\vec{k}$.

The functional relationship between the index of refraction $n$ and the scattering amplitude $f(k, \theta)$ can be obtained using the optical theorem[8]. This relates the scattering cross section to the imaginary part of the scattering amplitude in the forward direction $\sigma = \frac{2\pi}{k_r} Im(f(k_r, 0))$ (where forward implies $\theta = 0$). Here $k_r$ is the relative (or center of mass) wavevector. Similarly, the phase shift is proportional to the real part of the scattering amplitude, $\phi = \frac{2\pi}{k_r} Re(f(k_r, 0))$. Finally, substituting these values into Eq. (2) gives

$$n(k_0) = 1 + \frac{2\pi N}{k_0} \left\langle \frac{f(k_r, 0)}{k_r} \right\rangle . \qquad (3)$$

This is the index of refraction for a particular incident wavevector ko. Since our target gas has a wide velocity distribution, this derivation shows that it is the bracketed quantity, $\langle ... \rangle$, that must be averaged for all center of mass wavevectors $k_r$. We calculate this average in a later section.

### II.1.2. $f(k, 0)$ as a sum over partial waves

Using assumptions of a spherically symmetric potential and probability conservation, it is possible to write the scattering amplitude as a sum over angular momenta or "partial waves"[8]:

$$f(k_r,\theta) = \frac{1}{k_r}\sum_{l=0}^{\infty}(2l+1)e^{i\delta_l}\sin\delta_l P_l(\cos\theta) \qquad (4)$$

where $\delta_l$ is the phase shift for angular momentum $l$. We restrict this to $\theta = 0$ for our purposes, in which case $P_l(1) = 1$. Separating the real and imaginary parts gives

$$\begin{aligned} Re(f(k_r,0)) &= \frac{1}{2k_r}\sum_{l=0}^{\infty}(2l+1)\sin 2\delta_l \\ Im(f(k_r,0)) &= \frac{1}{2k_r}\sum_{l=0}^{\infty}(2l+1)2\sin 2\delta_l \qquad (5) \end{aligned}$$

The maximum angular momentum quantum number, $l_{max}$ that contributes to this sum can be found by equating $\hbar l_{max}$ with $\hbar k_r b_{max}$ where $b_{max}$ is the maximum impact parameter at which the potential is significant. In experiments at thermal energies ($\sim 0.1$ eV), a minimum of a few hundred partial waves contribute to this sum.

Because such a large number of angular momenta contribute, we are justified in using a semiclassical approach where we convert the sum over angular momenta into an integral over impact parameter $b$, where $l \rightarrow bk_r$ and $\delta_l = rig\delta(b,k_r)$. So we have

$$\begin{aligned} Re(f(k_r,0)) &= k_r\int_0^{\infty} bdb\sin 2\delta(b,k_r) \\ Im(f(k_r,0)) &= 2k_r\int_0^{\infty} bdb\,\sin^2\,\delta(b,k_r) \qquad (6) \end{aligned}$$

In some cases, such as a $1/r^n$ potential, this tremendously simplifies the calculation of the scattering amplitude. We will see that it is the ratio of these two quantities $Re(f(k,0))/Im(f(k,0))$, which we will refer to simply as Re/Im, that gives the best theoretical insight and is also the ideal experimental quantity to measure.

### II.1.3. Analytical results for $f(k,0)$

An analytic result can be obtained for Re/Im for the special case $V(r) = -C_n r^{-n}$. In general, these calculations have two steps: calculate the partial wave phase shifts, which are a function of the interatomic potential $V(r)$, and then calculate Re/Im as a function of the phase shifts. The partial wave phase shifts in the eikonal approximation (i.e. assuming a straight-line trajectory through the potential along $z$ with $r = \sqrt{z^2+b^2}$) for impact parameter $b$ and relative wavevector $k_r$ are

$$\delta_n(b,k_r) = \frac{-1}{\hbar v}\int_{-\infty}^{+\infty} V(z)dz = \frac{-\mu}{k_r\hbar^2}\int_{-\infty}^{+\infty} -C_n r^{-n}dz\ . \qquad (7)$$

The result of this integration is

$$\delta_n(b,k_r) = \frac{c_n'\pi\mu C_n}{k_r\hbar^2 b^{n-1}} \quad \text{where} \quad c_n' = \frac{1.3.5...(n-3)}{2.4.6...(n-2)}\ . \qquad (8)$$

We can now integrate the real and imaginary parts off separately using this result for the phase shifts. The integration requires a change of variables from $b$ to $\delta$, where from Eq. (8) $b = (c_n'\pi\mu C_n/k_r\hbar^2)^{1/(n-1)}\delta^{1/(1-n)}$. This gives

$$Re(f) = k_r\int_0^{\infty} b\,\sin(2\delta)db = \left(\frac{c_n'\pi\mu C_n}{k_r\hbar^2}\right)^{2/n-1}\frac{k_r}{n-1}\int_0^{\infty}\delta^{1+n/1-n}\sin(2\delta)d\delta\ . \qquad (9)$$

The result of the integration is

$$Re(f) = \left(\frac{c_n'\pi\mu C_n}{k_r\hbar^2}\right)^{2/n-1}\frac{k_r}{4^{n-2/n-1}}\Gamma\left(\frac{n-3}{n-1}\right)\ \sin\left(\frac{\pi}{n-1}\right)\ . \qquad (10)$$

Similar steps applied to the imaginary part of $f$, give the result

$$Im(f) = \left(\frac{c_n' \pi \mu C_n}{k_r \hbar^2}\right)^{2/n-1} \frac{k_r}{4^{n-2/n-1}} \Gamma\left(\frac{n-3}{n-1}\right) \sin\left(\frac{\pi}{n-1}\right) . \quad (11)$$

We therefore arrive at the following simple result for the special case $V(r) = -C_n r^{-n}$:

$$\frac{Re(f)}{Im(f)} = \tan\left(\frac{\pi}{n-1}\right) . \quad (12)$$

This derivation relies on the potential being strong enough that many (i.e. several hundred) phase shifts contribute significantly. It will only work for real potentials if the potential is well represented by this $r^{-n}$ form into the point where it gives a phase shift of many radians. Moreover, it neglects the effects of glory scattering where, because the real potential has a minimum, the derivative of the phase with respect to impact parameter is zero.

An exact analytical result can also be obtained for the partial wave phase shifts for the case of hard sphere scattering with radius $r_H$[8]. However, the integration over partial wave phase shifts to calculate Re and Im is not analytic. Numerical calculations reveal that the ratio of real to imaginary parts is $\approx -1/\sqrt{k_r r_H}$ [3], that is one over the square root of the number of partial waves involved in the scattering. The negative ratio is indicative of the repulsion due to tunneling experienced by the few partial waves whose classical impact parameter is near $r_H$.

### II.1.4. Numerical calculation of $f(k,0)$

A numerical calculation of the integrands of Eq. (6), $b \sin 2\delta$ and $b \sin^2\delta$, provides insight into the real and imaginary parts of the scattering amplitude. We have performed this calculation using a typical interatomic potential for the sodium-argon system[9] (Fig. (2)). This potential has a Born-Mayer exponential repulsive core and a van der Waals expansion for the long range attractive part. That is

$$V(r) = Ae^{-br} - \left(\frac{\frac{C_6}{r^6} + \frac{C_8}{r^8} + C_{10}}{r^{10}}\right) g(b,r) \quad (13)$$

where the $C_6$ arises in second order perturbation theory from the dipole-dipole interatomic interaction term, $C_8$ the dipole-quadrupole, and $C_{10}$ the dipole-octupole and quadrupole- quadrupole terms. If $g(b,r) = 1$, Eq. (13) diverges to $-\infty$ for small $r$ because of the dispersion terms. Various schemes are used to slowly "turn off" these terms at small $r$ to regularize the potential[6,9,10]. We used the method of Ref. [6], where $g(b,r)$ is proportional to incomplete gamma functions.

To calculate the real and imaginary parts of the scattering amplitude for this system, we must first calculate the phase shifts in the integrands of Eq. (6). We have

$$\delta(b,k_r) = \frac{-\mu}{k_r\hbar^2}\int_{-\infty}^{\infty} V(r)dr = \frac{-\mu}{k_r\hbar^2}\int_{-\infty}^{\infty} V\left(\sqrt{b^2+z^2}\right) dz . \quad (14)$$

This calculation is shown in Fig. (3) using the potential of Fig. (2) and center of mass energies 0.01 eV, 0.1 eV (which is typical for sodium beam velocity of $\sim$1000 m/sec) and 1.0 eV. We then calculate the integrands of the real and imaginary parts of $f$, $b \sin 2\delta$ and $b \sin^2\delta$, which are presented in Fig. (4) for the same center of mass energies.

The following observations about $Re(f)$ and $Im(f)$ are general and would apply for any reasonable potential. The imaginary part (bottom of Fig. (4)) averages to a line with slope 1/2 for smaller impact parameters, indicative that this part of the potential contributes to the total cross section. The real part averages out to zero for small impact parameters so most of the contribution to this integral comes only from the long range

part of the potential. This shows why the ratio Re/Im gives a good indication of the long range part of the potential.

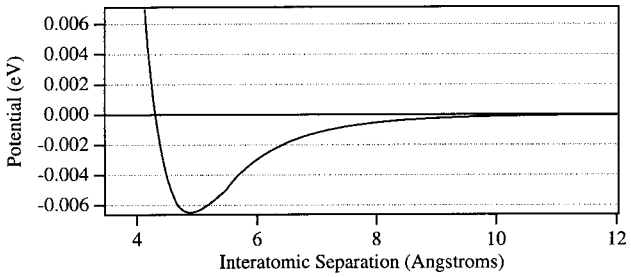


Figure 2. The Na-Ar interatomic potential from Ref. [9]. The well depth is slightly over 6 millieV and the equilibrium interatomic separation is 4.9Å.

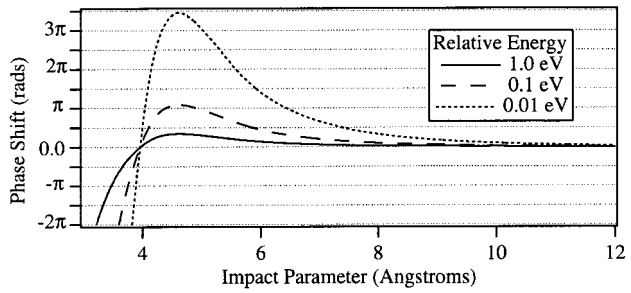


Figure 3. Phase shift as a function of impact parameter for the potential of Fig. (2) and 0.01, 0.1, and 1.0 eV center of mass energies. The peak phase is slightly over $\pi$ radians for 0.1 eV at about 4.5 Å.

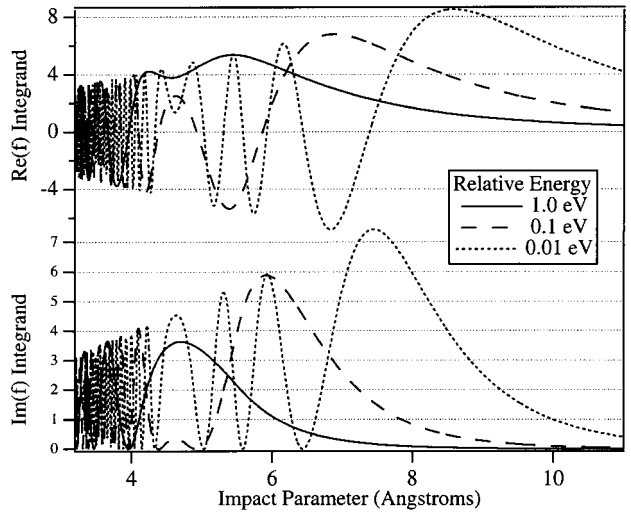


Figure 4. Integrands of the real (top) and imaginary (bottom) parts of the forward scattering amplitude. The rapidly oscillating parts at small impact parameters average to zero for the real part but to a positive value for the imaginary part. Note the non-oscillating structure at b=4.6 Å. This comes from a stationary point in $\delta(b)$ and gives rise to glory scattering.

For potentials, like ours, with reasonable minima there is glory scattering - which results when the stationary point of the phase $\delta(b)$ (near the well minimum at $b = 4.6$ Å in Fig. (4)) - makes an additional contribution to the integrands for $Re(f)$ and $Im(f)$. Since this contribution can add to or subtract from the magnitude of the real and imaginary parts, depending on the center of mass energy, we expect to see additional structure (which generally oscillates) in plots of Re/Im as a function of energy that is dependent on the potential well shape.

We have utilized the eikonal approximation and the assumption of a straight line trajectory in these calculations thus far. We can also calculate Re/Im numerically by defining a critical impact parameter $b_c$, above which the eikonal method with a straight line is very accurate and below which we sum over partial waves, using the JWKB method to calculate the partial wave phase shifts. This method was used for the results presented here. Thus we calculate

$$Re \text{ or } Im = \sum_{l=0}^{l_{\max}=k_r b_c} + \int_{b_c}^{\infty} db \ . \qquad (15)$$

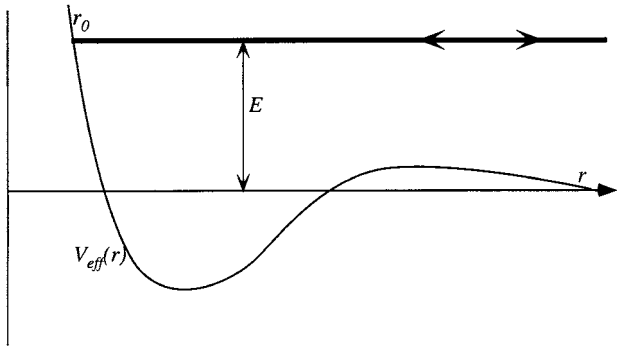


Figure 5. Schematic showing the range of integration for the JWKB method. The effective potential is defined in the text, the center of mass energy is $E$, and the inner turning point is shown. The eikonal method would be used for impact parameters greater than the cutoff radius.

The JWKB approximation for the phase shift is valid in regions where the potential does not change much on the scale of the wavelength. Near classical turning points where this breaks down, standard connection formulas are used that account for exponential decay into the forbidden regions. The result is an accurate method for computing the phase shift. Consider the geometry of Fig. (5). We have an effective potential

$$V_{eff}(r,l) = V(r) + \frac{\hbar 2l(l+1)}{2\mu r^2} \tag{16}$$

and the classical turning point $r_0$ for an energy $E$ is shown. We need to calculate the JWKB phase from infinity into the turning point (a Newton's method algorithm is used to find this point) and then back out to infinity. The result is

$$\delta_{JWKB}(l,k_r) = \frac{\sqrt{2\mu}}{\hbar}\int_{r_0}^{\infty}\sqrt{E - V_{\rm eff}(r,l)}dr + \frac{\pi}{2}l - k_r r_0 + \frac{\pi}{4} \tag{17}$$

Using these partial wave phase shifts the summation in Eq. (15) can be computed.

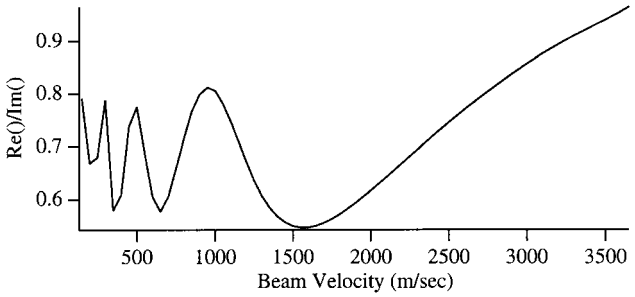


Figure 6. The resulting ratio as a function of incident beam energy for the potential of Fig. (2). Each point plotted here requires the full calculation of Eqn. (15) for the specified center of mass energy.

For the realistic potential of Fig. (2) of the Na-Ar system, we have calculated the ratio Re/Im as a function of incident beam energy or, equivalently, center of mass wavevector $k_r$, using this technique. The result is shown in Fig. (6). This calculation still assumes a fixed target gas, that is, the gas is at a temperature of zero Kelvin. The most noteworthy feature is the oscillatory structure of this curve which arises primarily from the stationary phase portion of the integral for the real part that occurs around b=4.6 Å (Fig. (4)). These are called "glory oscillations" or "glory undulations" when they occur in the total cross section - they are more pronounced in $Re(f)$ than in $Im(f)$, showing the increased sensitivity of the index of refraction to glory effects.

### II.1.5. Velocity averaged $f(k,0)$

Having calculated values of $f$ for particular center of mass wavevectors $k_r$, we now must average over the actual velocity distributions to compare with experimental data. The experiments performed to date have typically involved a room temperature ( 300K) target gas and an internally cold projectile beam with 7% rms velocity width. To compute the predicted Re/Im, (see Eq. (3)) we must perform the average

$$\left\langle \frac{f(k_r,0)}{k_r} \right\rangle = \int_0^{\infty} \frac{1}{k_r} f(k_r,0)\rho(E)dE = \frac{\hbar^2}{\mu}\int_0^{\infty} f(k_r,0)\rho(k_r)dk_r \tag{18}$$

which in turn requires knowledge of the distribution $\rho(E)$ for the center of mass energy $E$. This has been derived for the case of a monochromatic incident beam[3,6]. For a beam with velocity $v_a$ and mass $m_a$ and a Boltzmann distributed target gas with mass $m_b$ and temperature $T$, the result is

$$\rho(E) = \sqrt{\frac{m_b}{2\pi k_b T}}\frac{2}{\mu\nu_a}\sinh\left(\frac{m_b\nu_a}{k_b T}\sqrt{\frac{2E}{\mu}}\right) e^{-\frac{m_b}{2k_bT}\left(\nu_a^2 + \frac{2E}{\mu}\right)} . \tag{19}$$

We have taken the further step of considering the impact of the velocity distribution of the atomic beam on this final averaging. We use the normalized "$v^3$-weighted" Gaussian that was experimentally verified for supersonic beams[11]. For an integrated beam intensity of $I$, the intensity at velocity $\nu_a$ is

$$i(\nu_a) = \frac{I\nu_a^3}{\sqrt{\pi}\alpha u^3\left(1+\frac{3}{2}\frac{\alpha^2}{u^2}\right)} e^{-(\nu_a - u/\alpha)^2} \ . \tag{20}$$

Here, $\alpha = \sqrt{2k_bT/m_a}$ is the characteristic particle velocity in the source oven (with temperature $T$). The enthalpy (sum of extemal and internal energy) per particle in the source oven is $\frac{\gamma}{\gamma-1}k_bT = \frac{5}{2}k_bT$ for a monatomic ideal gas, and this gets fully transferred adiabatically into the kinetic energy $\frac{1}{2}m_au^2$ of the beam during the supersonic expansion. Thus, $u = \sqrt{5k_bT/m_a}$ is the predicted velocity of the beam. Finally, integrating over the velocity distribution of the source $\int \rho(E,\nu_a)i(\nu_a)d\nu_a$ yields

$$\rho(E) = \sqrt{\frac{m_b/8\pi k_bT}{\mu\alpha u^3\left(1+\frac{3}{2}\frac{\alpha^2}{u^2}\right)}} e^{-\left(\frac{m_bE}{\mu k_BT}+\frac{\mu^2}{\alpha^2}\right)} C_0^{-\frac{5}{2}} e^{\frac{C_1^2+C_2^2}{4C_0}} \left[(2C_0+C_1^2+C_2^2)\sinh\left(\frac{C_1C_2}{2C_0}\right) + 2C_1C_2\cosh\left(\frac{C_1C_2}{2C_0}\right)\right]$$

where

$$C_0 = \frac{1}{\alpha^2} + \frac{m_b}{2k_bT} \ ,$$

$$C_1 = \frac{m_b}{k_bT} + \sqrt{\frac{2E}{\mu}} \ , \text{and} \tag{21}$$

$$C_2 = \frac{2u}{\alpha^2} \ .$$

This result reduces to Eq. (19) in the limit that velocity width goes to zero, $\alpha \to 0$. This normalized velocity distribution is plotted in Fig. (7) for a variety of target gases and for 0% and 10% beam velocity widths. The effects of averaging over the beam's velocity width is substantial only for heavier target gases.

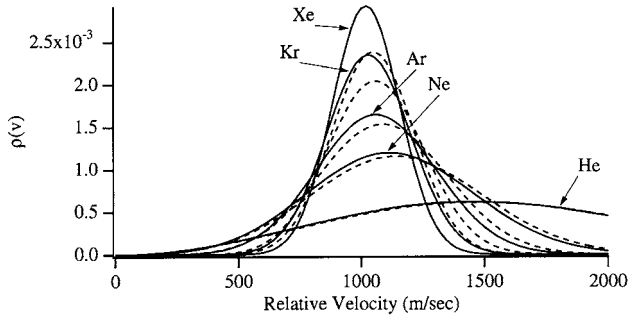


Figure 7. Normalized center of mass velocity distributions. The incident beam is sodium atoms at 1000 m/sec with the rms velocity widths of 0% (solid) and 10% (dashed). The target temperature is 300K.

Using this velocity averaging, we find that the large amount of structure or curvature in the ratio plotted in Fig. (6) will be significantly damped out for room temperature gases (300K). Fig. (8) includes the requisite velocity averaging for a 300 Kelvin target. (The curve from Fig. (6) is included, for comparison purposes.)

Two other curves on this figure show the sensitivity of Re/Im to changes in the long-range van der Waals coefficients. The Cn-coefficients were altered by +10% while the coefficients of the repulsive core were altered in such a way as to leave the well depth and position unaltered. The general effect is to raise/lower the whole curve by a few percent for a 10% change in the coefficients.

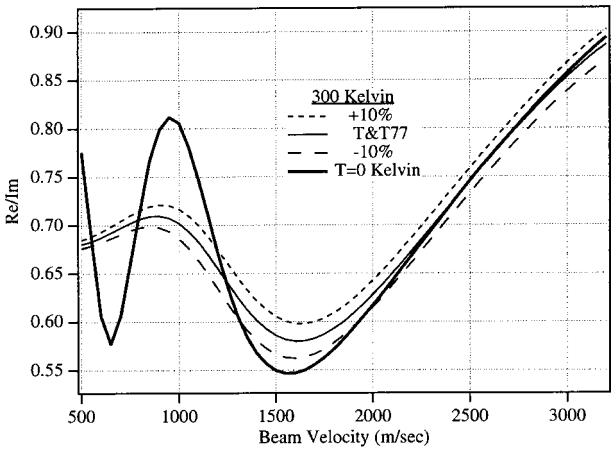


Figure 8. Velocity averaged ratio of real to imaginary parts of the scattering amplitude for a sodium beam with the specified velocity passing through a 300 Kelvin argon target gas. (For comparison purposes, the dark solid line is the T=0 case from Fig. (6)) Light solid line is the potential from Ref. [9]. Dotted lines use this potential but uniformly increase/decrease the van der Waals coefficients. The repulsive core coefficients were altered to fix the well in the same place as Ref. [9].

## II.2. Experiment

### II.2.1. Introduction

Measuring Re/Im for a large range of velocities, (Fig. (8)) required three major experimental modifications to our atom interferometer: use of gratings with sub-200 nm period caused larger diffraction angles and thus larger separation of the two beams at the gas cell; an exceptionally flat dividing barrier (septum) placed between the two atomic beam paths permitted measurements when the separation of the two beams in the interferometer was only 25 microns, allowing us to take data at higher velocities where the atom diffraction angle was less; and a unique gas handling system for our source produced an atomic beam in which the velocity could be reproducibly adjusted. In previous experiments, 200nm gratings and a larger septum width limited the velocity to less than 1600 m/sec, but with this thinner septum and finer gratings we can now fully separate ~3000m/sec beams. (Higher velocities have a smaller diffraction angle and are less well separated.)

### II.2.2. Technical advances in the interferometer

Amplitude diffraction gratings, manufactured in a thin silicon nitride membrane using an electron beam lithography technique, are the essential elements of our atom interferometer. We recently developed a registration technique to reduce thermal drifts in the lithography stage of the grating manufacture[12]. This resulted in 140nm period gratings with very good overall dimensional register which replaced the 200nm period gratings we used in all previous interferometer work.

The second advance was the construction of the new gas cell with a thinner, flatter membrane to keep the gas localized on one side of the interferometer. The key was the use of a thin ($\sim$ 10 $\mu$m) wafer of single crystal silicon as the dividing wall which was bonded to a piece of glass in which a gas cell had already been cut out (See Fig. (9)). This single sided interaction region using a rigid septum had fewer components and greater overall mechanical ruggedness. Our previous interaction regions[13] consisted of a thin foil stretched flat between two metal plates, but offset by spacers so that it was free-standing. The new interaction region extended only about 5 cm along the beam in contrast to the 10 cm of the earlier design.

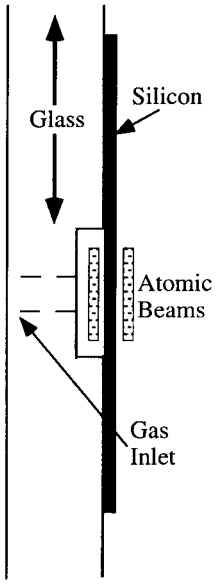


Figure 9. Cross section of the interaction region as seen by the approaching atomic beams, which pass on either side of the dividing wall (septum). The glass has a channel cut lengthwise through it and a small hole to let the gas in (from the left in the Figure). The silicon wafer is on ~10 $\mu$m thick and- is bonded to the glass, which is 5-8 mm thick.

Third, we used two carrier gases continuously mixed together to produce a broad range of sodium beam velocities. The velocity of the sodium beam is determined by

$$\nu = \sqrt{\frac{5k_BT}{\bar{m}}} \tag{22}$$

and

$$\bar{m} = \frac{m_a p_a + m_b p_b}{p_{\text{total}}} \ ,$$

where $m$ and $p$ stand for the mass and partial pressure of the sodium vapor and the inert carrier gas mixture inside the source oven at temperature $T$. By varying the mass of a single inert carrier gas from helium all the way up to xenon, we can change this velocity by about a factor of six (Fig. (10)). To get intermediate velocities, we simply mixed two species of gas. We used a gas proportioning system to control the flow rate of the two different carrier gases, and demonstrated that by selecting appropriate flow rates, we can reproducibly select a sodium velocity which was accurately determined from single grating diffraction patterns. (See Ref. [2] for further details).

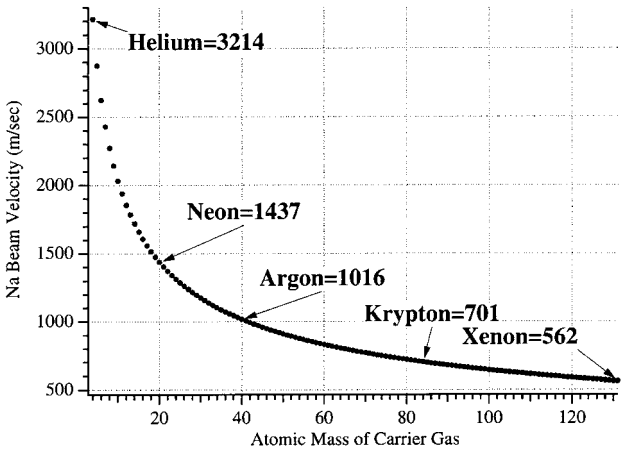


Figure 10. Beam velocity as determined by the mass of the carrier gas. A source temperature of 1000 K is assumed.

### II.2.3. Results: the velocity dependence of the index of refraction

With our experimental technique it is the ratio Re/Im that we most sensitively measure, because the gas density $N$ in this ratio cancels out. In general, gas density is a difficult experimental parameter to measure. The cancellation is seen by considering an atomic interference fringe in which both the phase and the amplitude is determined. If the wave that travels outside the gas cell (the gas density is zero) has amplitude $A_0$, and the wave that travels inside the gas cell has an amplitude that depends on the gas density $N$, $A_i(N) = A_i(0)e^{\sigma NL}$, then the interference of these two waves gives $A_0^2 + A_i(N)^2 + 2A_0A_i(N)\cos(k_g x + \phi)$. The amplitude of the atomic interference fringe is $2A_0A_i(N)$ which, normalized to the case where there is zero gas in the cell ($N = 0$), is

$$A_i(N)/A_i(0) = e^{-\sigma NL} \ . \qquad (23)$$

Now, if we examine the ratio of the phase shift to the natural logarithm of $A_i(N)/A_i(0)$, we find

$$\frac{-\phi}{\ln(e^{-\sigma NL})} = \frac{(-2\pi Re(f(k_r,0))/k_r)NL}{(-2\pi Im(f(k_r,0))/k_r)NL} = \frac{Re(f(k_r,0))}{Im(f(k_r,0))} \qquad (24)$$

Because $N$, the number density of the gas, cancels out in this equation, we always measure the ratio of the phase shift over the log of the fringe amplitude in our experiments.

Our experiments focused on measuring Re/Im for an argon target gas and an incident sodium beam with numerous beam velocities spanning the range ~1100 m/sec to ~2800 m/sec. For each velocity, the interference fringes were measured while alternately leaking argon gas into the cell and then allowing it to leak out. That is, we recorded both the phase shift $\phi$- given by the difference in phase when gas is present and when there is no gas - and the fringe amplitude, normalized to the case of no gas, $A_i(N)/A_i(0)$. We can then determine Re/Im using Eq.(24). This alternation between gas and "no gas" must be repeated on a relatively short time scale, i.e. every few minutes, because the phase in our interferometer drifts on the order of 0.1 rad/minute. Because of this drift, and because we can't record gas and "no gas" data at the same instant in time, a low order polynomial is fit to the "no gas" phase and amplitude data as a function of time to estimate the actual "no gas" values during the time the gas was present.

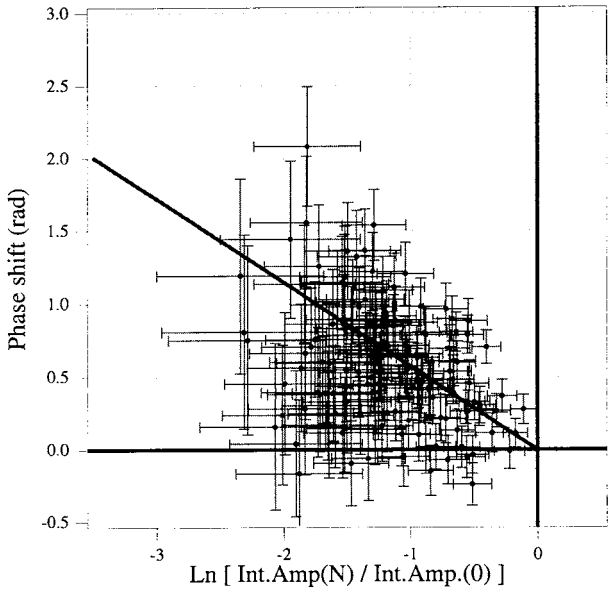


Figure 11. Each data point represents an interference fringe from 10 seconds of data. The 30 minutes of data shown (~180 points), with appropriate error bars in both dimensions, are taken with a single velocity of the atomic beam. A least squares linear fit determines the slope of the line (and hence the ratio Re/Im) to about 4% for this velocity. A similar data set is taken for each velocity of the atomic beam.

We switched between gas and no gas until ~30 minutes of data had been acquired. The fringe phase shift, $\phi$, and amplitude, $A_i(N)/A_i(0)$, were recorded for each 10 seconds of data. If we plot these points on a graph of $\phi$ versus $ln(A_i(N)/A_i(0))$ (Fig. (11)), the slope of a

least squares linear fit that passes through these points and the origin (by definition, there is zero phase shift when there is no gas in the cell ($N = 0$)) is, according to Eq. (24), the ratio Re/Im. This is repeated for each velocity of the sodium beam. When we combine several runs for a particular velocity (often taken on different days), typical statistical error bars are 3-5%. However, the 15% discrepancy with our earlier data on Na-Ar at around 1030m/s[3], together with a similar discrepancy with the theoretical predictions discussed below suggest that our data may be systematically high by roughly this amount. Several sources of experimental error have been considered. The data reported here were taken with a detector whose sensitivity was fading throughout the run, so the normalization of the fringe amplitude by the "no gas" amplitude $A_i(0)$ is particularly important. Other errors, including differences in the interaction regions, were considered but are all incapable of explaining systematic effects of this magnitude in our measurement of $Re(f)/Im(f)$[2].

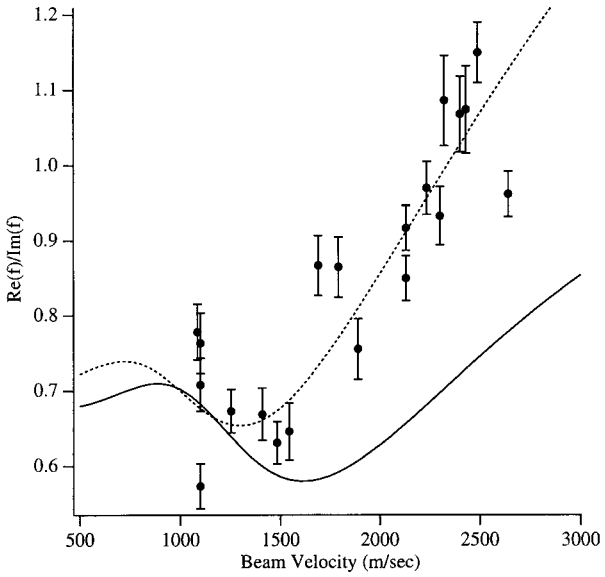


Figure 12. The final results of numerous data scan at many different sodium beam velocities. The solid line is the theory of Ref. [9]. At higher velocities, the disagreement is particularly large. The dashed line uses Ref. [9] with the well depth decreased 30% and the minimum position decreased 15%. Possible changes in the theoretical interatomic potential are discussed in the text as well as future experimental prospects for reducing the error bars on the data.

This type of analysis was performed for many different sodium beam velocities on several different days with several different interferometer alignments. These results are summarized in Fig. (12) although, as noted above, they are notably higher than the theoretical predictions made with Ref. [9], especially at higher velocities. However, they show a strong velocity dependence that is outside the bounds of any likely systematic error and is also in good accord with the predicted shape of the glory oscillation.

### II.2.4. Discussion

In order to explore the sensitivity of this new type of measurement to the potential, we have made modifications to the sodium-argon potential $V(r)$ of Ref. [9] to attempt to fit this new data. In general, we found that movement of the well position to a shorter radius and a shallower depth raised the predicted ratio of Re/Im. One potential that qualitatively fits our data, has a 30% shallower well and 15% shorter radius than Ref. [9]. (Movement of the radius affected the results about twice as strongly.) These changes to the well position exceed the variability found in Na-Ar potentials deduced in various ways in the literature which show variation of nearly 20% in the well depth and 5% in the position. This (dashed) curve is shown in Fig. (12). The error bars on the data are currently too large to distinguish subtle variations of the potential shape. Work is underway to account simultaneously for total and differential cross section measurements and spectroscopic measurements of bound states for Na-Ar molecules, including dissociation energies and vibrational spectra, to constrain these otherwise arbitrary changes in the interatomic potential. This should come close to finding the true Na-Ar interatomic potential.

This experiment was the first to observe glory structure in the velocity dependence of the index of refraction of atomic de Broglie waves. We utilized a new tool - the atom interferometer - that is able to measure the scattering induced phase shift in an atom wave. Several experimental modifications are underway: the target cell is going to be cooled to 77K to retain more of the glory oscillation amplitude in the predicted theory, the interferometer is being rebuilt so as to minimize vibrations and zero phase fluctuations, and more optimal atom diffraction gratings will be used. (Straightforward changes to the detector and gratings are expected to improve our signal by a factor of 3-4.) With future data, new constraints are expected to be applied to the determination of sodium-noble gas potentials.

## III. Fundamental studies of coherence loss

Interferometers of all types have had application to fundamental problems and precision tests of physical theories, especially quantum mechanics, and atom interferometers are sure to continue this tradition. In this section we focus our attention on the fundamental question, "what limits do the size and complexity of particles place on the ability of their center of mass motion to exhibit interference effects?" Quantum mechanical treatment of the center of mass motion of increasingly complex systems is an important theme in modern physics. This issue is manifest theoretically in studies of the transition from quantum through mesoscopic to classical regimes and experimentally in efforts to coherently control and manipulate the external spatial coordinates of complex systems, as exemplified by the wide interest in matter wave optics and interferometry. As demonstrated in our recent work[14,21], matter wave optics and interferometry have been extended to atoms and molecules – systems characterized by many degenerate and non-degenerate internal quantum states.

In this section we will investigate if and where there might be limits – in theory or in practice – to coherent manipulation of the center of mass motion of larger and more complex particles due to the interaction of radiation with the particle as it is passing through the interferometer. The key result here is our experimental realization of a *gedanken* experiment suggested by Feynman, in which one attempts, through the scattering of a single photon, to determine (i.e. Iocalize) on which side of the interferometer an atom passes. We then consider the question of what happens to the coherence that is lost when the particle passing through the interferometer interacts with this radiation. We will demonstrate that the coherence becomes entangled with the scattered radiation – and show that this coherence can be regained by selectively detecting atoms that scatter this radiation into a restricted subspace of all possible final directions.

### III.1. Coherence loss due to scattering a single photon – discussion

The principle that a system can be in a coherent superposition of different states and exhibit interference effects is a fundamental element of quantum mechanics. Immediately, the question arises as to what happens to the interference if one tries to determine experimentally which state the system is in. This is the basis of the famous debate between Bohr and Einstein, in which they discussed *Welcher-Weg* ("which way") information in the Young's double slit experiment[22–25]. In a more recent *gedanken* experiment suggested by Feynman, a Heisenberg light microscope is used to provide Welcher- Weg information in a Young's double slit experiment with electrons[23] or atoms[26,27]. In this section, we will discuss our experimental realization of this *gedanken* experiment using our atom interferometer.

One starting point is the principle of complementarity. Since the contrast of the interference fringes we observe in our interferometer is a measure of the amount of the atomic coherence, complementarity demands that the fringes must disappear when the slit separation (more generally the path separation at the point of measurement) is large enough so that, in principle, one could detect through which slit the particle passed[28] using a Heisenberg microscope. Since the loss of contrast is related to the possibility of measuring the atom's position, for example by observing a photon scattered from the atom, it is necessary to consider a quantum treatment of this measurement process. The measurement interaction considered here is the elastic scattering of the photon by the atom, which causes their initially separable wave function to evolve into an entangled state[29] – a sum of separable wave functions, each of which conserves the total momentum and energy of the system, and which can no longer be written as a product of separate atom and photon wave functions. This entanglement can result in a loss of atomic coherence when information about the scattered photon is disregarded. The effects of such entanglement are relevant to important issues in contemporary quantum mechanics, including EPR type correlations, understanding of the measurement process, and the loss of coherence in the passage from quantum to classical mechanics. The experiment presented here reveals the details of the loss of coherence of one system due to entanglement with another. This is accomplished by scattering a probe particle off an interfering superposition of the observed system as it passes through an interferometer.

We now discuss experiments we performed to measure the loss of atomic coherence due to scattering single photons from sodium atoms inside our interferometer. Our experiments[30] demonstrate that the loss of coherence may be attributed to the random phase difference between the two arms of the interferometer which is imprinted on the atom during the scattering process. This random phase depends fundamentally on the spatial separation of the interfering waves at the point of scattering, relative to the wavelength of the scattering probe.

Our experiments also address the question: "where is the coherence lost to and how may it be regained?" Although the elastic scattering of a photon produces an entangled state, it is not per se a dissipative process and may be treated with Schrödinger's equation without any *ad hoc* dissipative term. Therefore the coherence is not truly lost, but rather becomes entangled with the scattered photon. Although the photon may be regarded as part of a measurement apparatus for determining the atom's position, it is here more naturally considered as a simple reservoir, consisting of the vacuum radiation modes accessible to it. We show the validity of this viewpoint by demonstrating that selective observation of atoms which scatter photons into a restricted part of the accessible phase space results in atomic fringes with regained contrast.

### III.2. Coherence loss due to scattering a single photon – experiment

To study the effects of photon scattering on the atomic coherence, single photons were scattered from the atoms passing through our three grating Mach-Zehnder interferometer (see Fig. (13)). The contrast (which measures the remaining coherence) and the phase of the interference pattern were measured as a function of the separation of the atom paths at the point of scattering[30].

In the absence of scattering, the atom wavefunction at the third grating may be

$$\psi(x) = u_1(x) + e^{i\varphi} u_2(x) e^{ik_g x} \tag{25}$$

where $u_{1,2}$ are (real) amplitudes of the upper and lower beams respectively, $k_g = 2\pi/d_g$ where $d_g$ is the period of the gratings, $\varphi$ is the phase difference between the two arms, and $x$ is a coordinate perpendicular both to the atomic beam and to the grating bars. To describe the effects of scattering within the interferometer, we first consider an atom elastically scattering a photon with well-defined incident momentum $k_i$ and final (measured) momentum $\vec{k}_f$, with $|\vec{k}_i| = |\vec{k}_f| = k_{\rm photon}$. After this well-defined scattering event, the atomic wavefunction becomes

$$\psi'(x) \propto u_1(x - \Delta x) + e^{i\varphi} u_2(x - \Delta x) e^{ik_g x + \Delta\varphi} \tag{26}$$

The resulting atomic interference pattern shows no loss in contrast but acquires a phase shift[31,32]

$$\Delta\varphi = \Delta\vec{k} \cdot \vec{d} = \Delta k_x d \tag{27}$$

where $\Delta\vec{k} = \vec{k}_f - \vec{k}_i$, and $\vec{d}$ is the separation between the two arms of the interferometer at the point of scattering. Eq. (26) implies that the photon recoil causes a spatial shift of the envelope of the atomic fringes by a distance

$$\Delta(x) = (2L - z)\Delta k_x / k_{\rm atom} \tag{28}$$

where $L$ is the distance between gratings, $k_{\rm atom} = 2\pi/\lambda_{dB}$ and $(2L - z)$ is the distance from the point of scattering to the third grating. Ehrenfest's theorem implies that this displacement is just the shift that a classical atom would experience due to the momentum transferred by the scattered photon.

In the case that the photon is disregarded, the atom interference pattern is given by an incoherent sum of interference pattems with different phase shifts corresponding to different final photon directions (i.e. a trace over the photon states),

$$C'\cos(k_g x + \Delta\varphi') = \int d(\Delta k_x) P(\Delta k_x) C_0 \cos(k_g x + \Delta k_x d) \tag{29}$$

where $P(\Delta k_x)$ is the probability distribution of transverse momentum transfer and $C_0$ is the original contrast or visibility of the atomic fringe pattern. For the case of scattering a single photon, $P(|dk_x)$ (shown in the inset to Fig. (14)) is determined by the radiation pattern of an oscillating dipole. The average transverse momentum transfer $\hbar\Delta k_x = 1\hbar k$ (a maximum of $2\hbar k$ occurs for backward scattering of the incoming photon and a

minimum of $0\hbar k$ occurs for forward scattering). Due to the average over the angular distribution of the unobserved scattered photons, there will be a loss of contrast ($C' \leq C_0$) and a phase shift $\Delta\varphi'$ of the observed atomic interference pattern. It follows from Eq. (29) that the measured contrast (phase) of the interference pattern as a function of the separation $d$ of the atom waves will vary as the magnitude (argument) of the Fourier transform of the probability distribution, $P(\Delta k_x)$. Eq. (29) is equivalent to the theoretical results obtained for the two-slit *gedanken* experiment[26,27] (where $d$ is identified with the slit separation), even though explicit which-path information is not necessarily available in our Mach- Zehnder interferometer because the atom wavefunctions can, and do, have a lateral extent (determined by the collimation of our atomic beam) much larger than their spatial separation at the point of scattering.

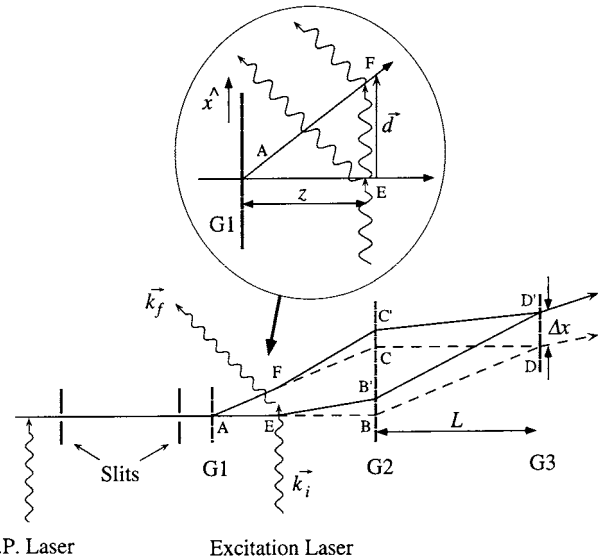


Figure 13. A schematic, not to scale, of our atom interferometer. The original atom trajectories (dashed lines) are modified (solid lines) due to scattering a photon (wavy lines). The inset shows a detailed view of the scattering process.

The atomic beam was first prepared in the $F = 2$, $m_F = 2$ state by optical pumping with a $\sigma^+$ polarized laser beam before the first collimating slit. We typically achieved $\sim$ 95% optical pumping, as measured by a two-wire Stem-Gerlach magnet which caused state-dependent deflections of the atomic beam. We employed a short laser interaction region, and adjusted the excitation field strength to scatter, on average a single photon from each atom, approaching this ideal case as closely as possible (Fig. (13)). The scattering cross section was maximized using $\sigma^+$ polarized laser light tuned to the D2 resonant line of Na ($\langle_{\text{photon}} =$ 589 nm) connecting the $F = 2$, $m_F = 2$ ground state to only the $F' = 3$, $m_{F'} = 3$ excited state. This ensured that the scattering left the atom in the same hyperfine state.

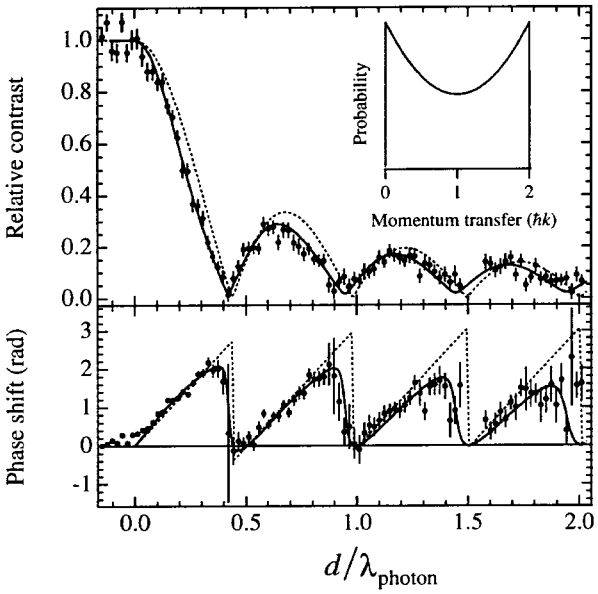


Figure 14. Relative contrast and phase shift of the interference pattern as a function of the separation of the interferometer arms at the point of scattering. The inset shows the angular distribution of spontaneously emitted photons projected onto an axis perpendicular to the atomic beam. The dashed curve corresponds to purely single photon scattering, and the solid curve is a best fit that includes contributions from atoms that scattered zero photons (4%) and two photons (14%).

The photons we wish to scatter from the atomic beam are provided by an excitation laser focused to a $\sim$15 $\mu$m waist (FWHM of the field) along the atom propagation direction. A cylindrical lens was used to defocus the beam perpendicular to the atom propagation direction to ensure unifomm illumination over the full $\sim$1 mm height of the atomic beam. The transit time through the waist was roughly one third of the lifetime of the excited state. Hence, the probability for resonant scattering in the two-state system exhibited weakly damped Rabi oscillations, which we observed by measuring the deflection of the collimated atomic beam as a function of laser power. To achieve one photon scattering event per atom, we adjusted the laser power to the first maximum of these oscillations, closely approximating a $\pi$-pulse.

The contrast and phase of the measured atomic interference patterns are shown in Fig. (14) for different path separations. The contrast was high when the separation $d$ at the point of scattering was much less than $\lambda_{\text{photon}}$ (corresponding to $\Delta k_x d \ll \pi$), but fell smoothly to zero as the separation was increased to about half the photon wavelength, at which point $\Delta k_x d \approx \pi$. (The zero would occur exactly at $d = \lambda_{\text{photon}}/2$ if the scattered photon angular distribution were isotropic.) As $d$ was increased further, a periodic rephasing of the interference gave rise to significant revivals of the contrast and to a periodic phase modulation.

The observed behavior of the contrast is consistent with the complementarity principle. Considering the photon scattering as a position measurement of the atom, complementarity suggests that the fringe contrast must disappear when the path separation is approximately half the wavelength of the scattered light, since this is the smallest distance that can be resolved by a perfect optical microscope. A more careful consideration of the imaging process of this scattered photon, however, reveals still richer behavior.

All optical imaging systems (even ideal ones, in which the lenses can capture every photon), produce images with diffraction rings. We consider using such a system to determine the origin of the photon scattered by the atom as it passes through the interferometer, and hence which path the atom took. If the bright central spot of the image were located on the upper arm of the interferometer, and another bright fringe of the diffraction rings coincided with the position of the lower arm, there would be significant uncertainty about the origin of the scattered photon. This uncertainty about the origin of the photon indicates a significant uncertainty about which path the atom took through the interferometer. Hence, when the separation $d$ between the two arms of the interferometer is such that the bright fringe of a diffraction ring centered on the upper arm falls on the lower arm, complementarity tells us that atomic interference, with reduced contrast, should re-occur. These revivals of contrast are indeed seen in the results of our experiment.

While the contrast generally decreases as $d$ increases, the phase shift $\Delta\phi$ of the fringes exhibits a sawtooth oscillation that is damped by the finite resolution of the apparatus. Starting at $d = 0$, $\Delta\phi$ increases linearly, with slope $2\pi$. This is the slope expected for momentum transfer of $1\hbar k$, the average momentum transfer of the symmetrical distribution (Fig. (14)). After each zero of the contrast, the sign of the interference pattern is reversed, subtracting $\pi$ from the phase and resulting in the observed sawtooth pattern.

In studying the decoherence and phase shift, we used a 50 $\mu$m wide detector (rhenium hot wire), which is larger than the deflection $\Delta x$ of the atom beam that results from the recoil momentum imparted by the scattered photon. The finite collimation of the atomic beam further degrades the overall momentum resolution of the apparatus. The result of this lack of resolution is that the measured interference patterns are averaged quite evenly over all values of $\Delta x$, which can be as large as 40 $\mu$m in our experiment – corresponding to displacement of the envelope of the fringe pattern by $\sim$200 fringes.

These numbers highlight the distinction between the expectation value of the atom's classical transverse position (the peak of the fringe envelope) and the phase of the fringes (which are never shifted by more than half a fringe). This distinction is emphasized by the fact that moving the point of scattering further downstream slightly reduces the displacement of the fringe envelope for a given $\vec{k}_f$, while monotonically increasing the corresponding phase shift. Therefore, the measured loss of fringe visibility cannot simply be understood as resulting from the transverse deflections of the atom at the detection screen (in our case the third grating) due to the photon momentum transfer, as it can be for the two-slit *gedanken* experiments.

The displacement of the envelope of the atom fringes, $\Delta x$, (or equivalently the $x$-component of the photon momentum transfer) is precisely what is measured in determining the transverse momentum distribution of an atomic beam after scattering a photon. These distributions have been measured for diffraction of an atomic beam passing through a standing light wave and undergoing a single[33] or many[18] spontaneous emissions, as well as for a simple collimated beam excited by a traveling light wave[17]. These results are usually discussed using a simple argument: the recoil momentum from spontaneous emission produces random angular displacements that smear the far-field pat-

tem, a viewpoint also applicable to two-slit *gedanken* experiments. Clearly the quantum phase shift measured in our experiment is distinct from the "deflection" of the atom $\Delta x$ due to the photon recoil. It reflects the phase difference of the photon wave function where it intersects the two arms of the interferometer.

The results here are also interesting as a contrast to the *gedanken* experiments recently proposed in which loss of contrast in an atom interferometer occurs after emission of a photon by the atom, even though there is insufficient momentum transfer to the wave function to explain this loss on the basis of dephasing[34]. In our experiment the opposite occurs: there is sufficient momentum transfer to the atom by the emitted photon to be easily detected, but the interference pattern is not destroyed for small separations. In both experiments the interaction with the radiation adds insignificant relative phase difference between the two arms of the interferometer. The crucial difference is that in the *gedanken* experiment of Ref. [34], the photon emitted by the atom is retained in one of two cavities located symmetrically on the two sides of the interferometer and can be used to determine which path the atom traversed (assuming the cavities were initially in number states), whereas in our experiment the scattered photon scatters without constraint and, for small d, no subsequent measurement can determine which path was traversed by the atom that scattered it. However, if a metal foil were interposed between the two sides of our interferometer (and a beamsplitter and mirrors added so that the laser beam was split and excited both sides coherently), detection of the scattered photon would then determine which side of the foil the atom traversed, and would destroy the interference pattern even though the phase shift imparted to the atoms was negligible, just as in Ref. [34].

### III.3. Regaining entangled coherence by selective observations

Returning to the loss of coherence induced by scattering of single photons from atoms in the interferometer, we now address the question: "where is the coherence lost to and how may it be regained?" We performed an experiment[30] to show that selective observation of atoms can result in fringes with regained contrast. This demonstrates that the coherence is not truly lost, but becomes entangled with the scattered photon which may be considered as a simple reservoir, consisting of the accessible vacuum radiation modes. When only atoms that scatter photons into a restricted part of this accessible phase space are observed, their distribution of possible phase shifts is narrower than without this selection, and they rephase more precisely and with greater coherence.

In this experiment, we observe atoms that are correlated with photons scattered into a narrow range of final directions. In principle, this could be achieved by detecting the photons scattered in a specific direction in coincidence with the detected atoms. With $\Delta k_x d$ now a known quantity, the predicted fringe shift would be the same for all the atoms (see Eq. (27)); consequently the fringe pattems of this restricted set of atoms would line up and no coherence would be lost. Unfortunately, such an approach is not feasible in our experiment for a number of technical reasons – principally the slow response of our atom detector and the inefficiency of available photon detectors.

Fortunately an alternative experimental approach is made possible by the fact that the change of momentum of the photon, $\hbar\Delta k_x$, is imparted to the atom, and can be measured by the atom's deflection (see Eq. (28)). Hence a measurement of an atom's $\Delta x$ gives the $\Delta k_x$ of the corresponding scattered photon. Furthermore, it is easily possible to measure $\Delta x$ in our three grating interferometer because (since we scatter the photons close to the first grating), the deflection of the envelope of the atomic fringes for a particular $\Delta k_x$ is 100 times larger than the associated fringe shift, $\Delta k_x d$. In practice this approach is superior to a correlation experiment because there are no inefficiencies or accidental coincidences introduced by the measurement of the scattered photon: the measurement of an atom's position reliably indicates the momentum transferred to that particular atom.

We have performed an experiment based on this technique to demonstrate the recovery of the entangled coherence. By using very narrow beam collimation in conjunction with a narrow detector, we can selectively detect only those atoms correlated with photons scattered within a limited range of $\Delta k_x$. This restricts the possible final photon states and results in a narrower

distribution $P'(\Delta k_x)$ in Eq. (29).

We performed experiments with recoil distributions centered on three different photon momenta. Fig. (15) shows three different realizations (referred to as Cases I-III) with the corresponding momentum transfer distributions, $P_i'(\Delta k_x), i = \text{I,II,III}$. The contrast is plotted as a function of $d$ for Cases I and III where we preferentially detect atoms that scattered photons in the forward and backward direction respectively. The contrast for Case II is similar to Case I and is not shown. The measured contrasts in this figure were normalized to the $d = 0$ (scattering laser on) values since a different number of atoms was detected with the laser off due to the absence of the deflection by the photons.

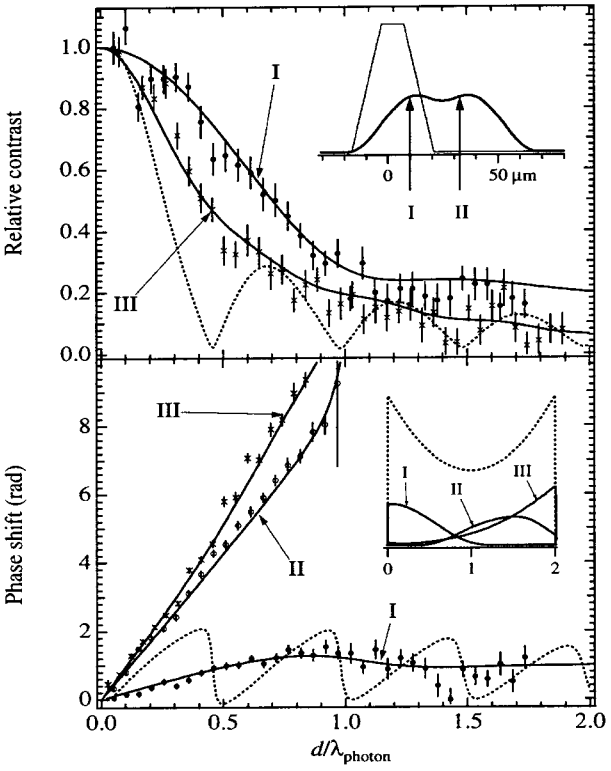


Figure 15. Relative contrast and phase shift of the interference pattern as a function of d for the cases in which atoms are correlated with photons scattered into a limited range of directions. The dashed curve is for uncorrelated atoms. The upper inset shows atomic beam profiles at the detector when the scattering laser is off (thin line) and when the laser is on (thick line). The arrows indicatethe detector positions for cases I and II. The lower inset shows the acceptance of the detector for each case compared to the original distribution (dotted line). Case I corresponds to predominantly forward scattered photons (minimal transfer of momentum), case III corresponds to backward scattered photons(transfer of two photon momenta), and case II lies in between.

Our results show that the contrast falls off much more slowly than previously – indeed we have regained over 60% of the lost contrast at $d \approx \lambda/2$. The contrast falls off more rapidly for a faster beam velocity (Case III, $v_{\text{beam}} = 3200$ m/s) than for the slower beam velocities (Cases I and II, $v_{\text{beam}} = 1400$ m/s). This is because, for a given $\Delta k_x$, a higher velocity atom beam will result in a smaller displacement $\Delta x$ at the third grating, resulting in diminished $\Delta k_x$ resolution.

The phase shift is plotted as a function of d for the three cases in the lower half of Fig. (15). The slope of Case III is nearly 411, indicating that the phase of the interference pattern is predominantly determined by the backward scattering events. Similarly, the slope of Case I asymptotically approaches a small constant value due to the predominance of forward scattering events. Case II is an intermediate case in which the slope of the curve, $\sim 3\pi$, is determined by the mean momentum transfer of $1.5\hbar k$. The lower inset shows the transverse momentum acceptance of the detector for each of the three cases (i.e. the functions $P_i'(\Delta k_x)$), which we determined using the known geometry and beam velocity. The fits for the data in Fig. (15) were calculated using Eq. (29) and the modified distributions $P_i'(\Delta k_x)$), and include effects of velocity averaging as well as the effects of those few atoms that scattered zero or two photons.

## IV. Inertial effects

Phase shifts caused by non-inertial motion of matter wave interferometers have been discussed by many authors in both non-relativistic and relativistic contexts (see for example Refs. [35-39]). Because such phase shifts increase with the mass of the interfering particle, atom interferometers are especially sensitive to inertial effects, and may be developed into rotation sensors, accelerometers, gravimeters, and gradiometers[39].

The inertial sensitivity of an atom interferometer arises because the freely propagating atoms form fringes with respect to an inertial reference frame. These fringes appear shifted if the interferometer moves with respect to this inertial frame while the atoms are in transit. To illustrate this, we now present a simple calculation of the fringe shift that results from acceleration a of a three grating interferometer in a direction perpendicular to both the grating bars and the atomic beam axis.

In a time $\tau = L/\nu$, where $L$ is the distance between gratings and $\nu$ is the velocity of the atom, the interferometer will move a distance $a\tau^2/2 = D/2$ (Fig. (16)). To simplify the calculation, we will make a convenient choice of initial transverse velocity $\nu_{\rm trans} == a\tau/2 = aL/2\nu$. Atoms in an accelerating interferometer which have this particular transverse velocity at the time they reach the first grating will pass through both the first and second gratings at exactly the same transverse positions as would atoms with *zero* transverse velocity moving in a *non-accelerating* interferometer. Because the atoms (or atom waves) in both cases intersect the first and second gratings at the same point, the relative phase shift between the two cases is given purely by the displacement of fringes at the third grating. Due to their transverse velocity, atoms form a fringe pattern at the third grating that is displaced by $\nu_{\rm trans}\tau = a\tau^2 = D$ from the axis of the interferometer at $t = 0$. However, when these atoms reach the third grating, the interferometer has now moved $a(2\tau)^2/2 = 2D$ from its original position, resulting in an apparent fringe shift of $-D$. This corresponds to a phase shift

$$\varphi_{\rm acceleration} = 2\pi\left(\frac{D}{d_g}\right) = 2\frac{2\pi}{d_g}\left(\frac{L}{\nu}\right)^2 a = -\frac{2\pi m^2 \lambda_{dB} A}{\hbar^2} a \qquad (30)$$

where $d_g$ is the period of the gratings, $\lambda_{dB} = h/m\nu$ is the de Broglie wavelength for an atom with mass $m$ and velocity $\nu$, and $A = L^2(\lambda_{dg}/d_g)$ is the area enclosed by the paths of the interferometer. It should be noted that the phase shift in our three grating geometry is independent of the mass of the particle, and was derived using classical physics.

The phase shift due to rotation of the interferometer (called the Sagnac effect) follows by noting that rotation with angular rate $\Omega$ gives rise to a Coriolis acceleration $\vec{a} = 2\vec{\nu} \times \vec{\Omega}$, allowing one to use Eq. (30) to calculate the phase shift due to rotation about an axis parallel to the grating bars,

$$\varphi_{\rm rotation} = \left[\frac{2\pi}{d_g}\left(\frac{L}{\nu}\right)^2 2\nu\right]\Omega = \left[4\pi\frac{mA}{h}\right]\Omega\ , \qquad (31)$$

where we call the bracketed factor the rotational response factor. This expression can also be directly obtained from considerations of the grating positions at the time of transit of the atoms through each grating[40].

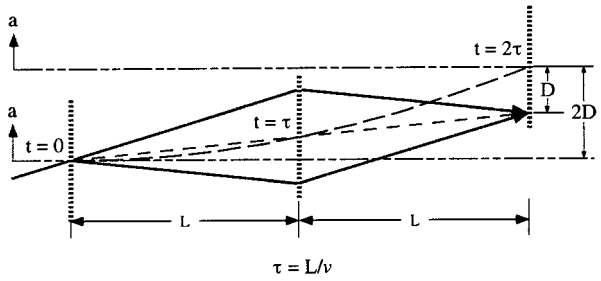


Figure 16. The interferometer in motion under the influence of a transverse acceleration. The atomic beam travels from left to right in the laboratory frame but interacts with the progressively displaced gratings of the movmg apparatus. Because a center-line (short dash) between the atom beam paths passes through the middle of the first grating at $t = 0$, and is offset by a transversevelocity $\nu_{\rm trans} = 1/2a\tau$, it also passes through the middle of the displaced second grating at $t = \tau$. The dashed curve (long dash) represents the displacement of the interferometer due to acceleration. The center-line of the accelerating interferometer is shown (short- long dash) at $t = 0$, and $t = 2\tau$ where fringes have a relative displacement of $-D$.

The results of the simple derivations above agree with the non-relativistic phase contributions derived by various more sophisticated methods[37−39]. The relativistic contributions to the phase shift caused by accelerations and rotations are of the order $E_{\rm kinetic}/mc^2$ smaller than the non-relativistic terms[36] and are unresolvable in our experiments.

The Sagnac rotational response factor is independent of the velocity of the particle in an interferometer in which the area is constant (as it would be for an interferometer employing conventional beam-splitters). However, since all demonstrated atom interferometers employ diffractive beam splitters, their rotational response factors will exhibit 1/v dependence. This dependence arises from the variation of the enclosed area which in turn results from the variation of the diffraction angle with velocity.

In contrast to rotations, the phase shift due to linear accelerations (see Eq. (31)) varies with velocity as $1/\nu^2$. Thus atom interferometers that use slow atoms will be relatively more sensitive to acceleration than to rotation.

Phase shifts due to rotation and acceleration, as well as shifts due to gravitational fields (which give the same response factor as acceleration due to the equivalence principle), have been observed in many kinds of matter

wave interferometers. Accelerations were measured using neutron interferometers[35,38], and using atoms[41]. The Sagnac phase shift for matter waves has been verified with accuracy on the order of 1% for neutrons[38,42] and electrons[43], and to about 10% for atoms using both interferometers[31,44] and classical Moiré regime atom optics[45].

In view of the numerous demonstrations of the sensitivity of matter wave interferometers to non-inertial motion, the motivation for such experiments is principally technological: can such devices become the sensors of choice in practical applications or can they demonstrate such high sensitivity that they open up new scientific possibilities? With these considerations in mind, the observation that the rotation-induced phase shift in an atom interferometer exceeds the Sagnac phase for light of frequency $\omega$ by an amount $mc^2/\hbar\omega$, typically $10^{10}$, suggests the tremendous potential of atom interferometer rotation sensor[39].

We now estimate the minimum angular velocities and accelerations detectable by our atom interferometer using the atomic velocity (1075 m/s) and signal intensity (a contrast of 12.9% and an rms count rate of 29 kcounts/sec) achieved in our apparatus. We assume that only Poissonian detection statistics degrade the signal-to-noise ratio, which is therefore proportional to $C\sqrt{N}$, where $C$ is the fringe contrast and $N$ is the total number of counts. The response factor for rotations is 1.86 rad/$\Omega_e$, with a corresponding (purely statistical) rotational noise of $\sim$35 m$\Omega_e$ in one second of integration time. (Note: one earth rate ($\Omega_e$) is $7.3 \times 10^{-5}$ rad/sec). For accelerations, the response factor is 116 rad/g, with a statistical noise of $\sim 5.5 \times 10^{-4}$ g in one second of integration time.

We performed experiments to measure both the response factor for rotation and the rotational noise of our interferometer. Both measurements were made by suspending the interferometer by a cable from the ceiling and then driving it with a sinusoidally varying force applied at some distance from the center of mass, thereby giving the interferometer a rotation rate $\Omega(t) = \Omega_0 \sin(2\pi f t)$.

The rotation rate $\Omega_0$ was typically several earth rates ($\Omega_e = 7.3 \times 10^{-5}$ rad/sec) for the response factor measurement, and about $\Omega_e/10$ for the noise measurements. For the response measurements, $f$ was chosen just over 1 Hz in order to minimize deformations of our interferometer (which has several prominent mechanical resonances in the 10 to 30 Hz frequency range). For the noise measurements, $f$ was around 4.6 Hz, where the measured residual rotational noise spectrum of the apparatus had a broad minimum.

Our procedure was to measure the acceleration at the sites of the first and third gratings of the suspended interferometer using accelerometers. While modulating the grating phase, ($\varphi_{\rm grating}(t) = k_g(x_1(t) - 2x_2(t) + x_3(t))$, with a sawtooth pattern at a frequency just less than 1 Hz, we recorded accelerations from both accelerometers, ($\varphi_{\rm grating}$ and the atom counts each millisecond. Readings from the accelerometers allowed us to infer the atom phase expected from the acceleration and rotation rate of the interferometer using Eqs. (30) and (31). We called this predicted inertial phase ($\varphi_{\rm predicted}$.

To study the magnitude and constancy of the response factor, we binned these data according to the $\varphi_{\rm predicted}$ determined from the accelerometer readings after suitable correction for their known frequency response. Since the frequency of the sawtooth modulation of ($\varphi_{\rm grating}$ was chosen to be incommensurate with $f$, the data in a bin with a particular value of ($\varphi_{\rm predicted}$ had a variety of values $\varphi_{\rm grating}$ allowing us to determine $\varphi_{\rm rotation}$. A plot $\varphi_{\rm rotation}$ vs. $\varphi_{\rm predicted}$ is shown in Fig. (17). The data reveal a linear response and an average response factor within error (0.8%) of that predicted from Eq. (31).

To study the reproducibility of our interferometer we employed a phase modulation technique to immediately convert atom counts into $\varphi_{\rm rotation}(t)$. This was accomplished by scanning the second grating (and hence ($\varphi_{\rm grating}$) at 1 Hz to produce a carrier modulation on the atom count rate. Since acceleration was negligible, the rotation of the interferometer introduced a phase modulation $\varphi_{\rm rotation}(t)$ to the carrier which was demodulated by homodyne detection, using both the sine and cosine of $\varphi_{\rm grating}(t)$ (measured by means of an optical interferometer with the same geometry as our atom interferometer) as the local oscillator.

From each of 21 data sets 32 seconds long, we analyzed samples of different sizes to find the rotation rate $\varphi_{\rm measured}(t)$ determined from the rotation phase

$\varphi_{\text{rotation}}(t)$ of the interferometer. Samples were taken from the middle of each data set and ranged in duration, $T$, from 0.66 to 10.66 seconds. Each sample was Fourier transformed and the magnitude of the amplitude of the rotation at the drive frequency $f$ was found. The rms fluctuations in the amplitudes for given sample lengths were then determined for the various averaging times, $T$. In Fig. (18) they are plotted and compared to the shot noise limit.

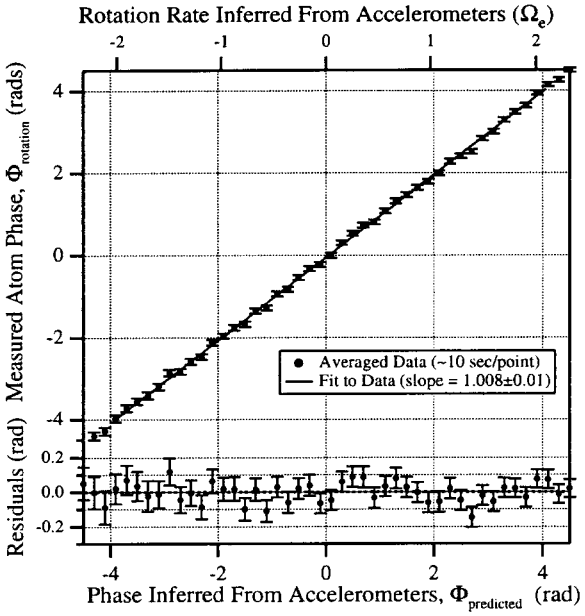


Figure 17. A plot of the measured interferometer phase, $\varphi_{\text{rotation}}$ verses the inferred phase from the accelerometer readings, $\varphi_{\text{predicted}}$ from a combination of 20 second runs totaling ~400 seconds of data (~10 seconds of data per point). There is a 0.8% difference between these measurements with a total error of 1%.

We attribute the excess noise of the interferometer relative to shot noise seen in Fig. (18), for $T$ greater than 2 seconds, to extraneous sources of rotational noise rather than to any intrinsic failure of atom interferometers. The observed noise $\Delta\Omega$ can be fit as an uncorrelated sum of shot noise, SNL, and background rotational noise, $B$, times an overestimation factor, $\alpha$,

$$\langle\Delta\Omega\rangle = \alpha\sqrt{SNL^2 + B^2} \qquad (32)$$

The over-estimation factor $\alpha = 1.09 \pm 0.02$, is close to unity, and is consistent with noise arising from imperfections in our modulation scheme together with the previous observation of super-poissonian noise from our detector. The background noise determined from the fit is $B = 10\ \text{m}\Omega_e \pm 1m\Omega_e$.

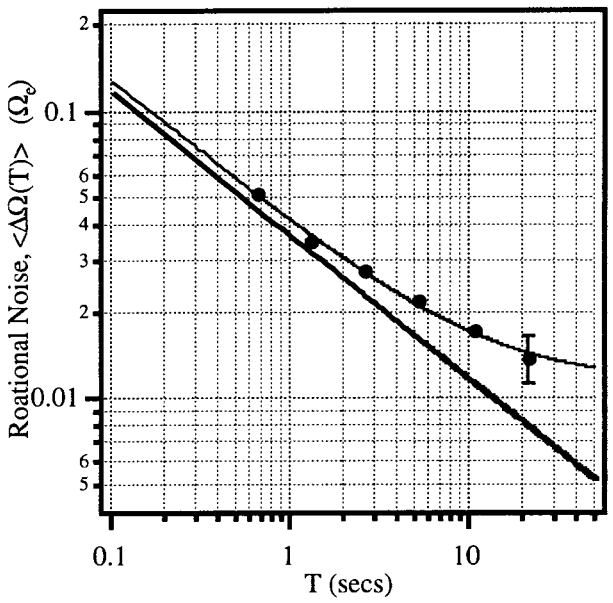


Figure 18. Reproducibility of the rotation rate measurements in the atom interferometer. Fluctuations in the spectral peak amplitude at the driving frequency, $f = 4.6$Hz (for 30 data sets), is compared to the predicted shot noise (dashed line) and plotted versus integration time, $T$. A fit to the data points with Eq. (32) yields an over-estimation factor $\alpha = 1.09 \pm 0.02$ and a background $B = 10\ \text{m}\Omega_e \pm 1m\Omega_e$.

We regard these results as highly encouraging for the future of inertial sensors using atom interferometers. Our interferometer was designed for separated beam interferometry, not inertial sensing. This resulted in restricting the usable area of our small 1 mm × 200 $\mu$m gratings at both ends of the machine by a combined factor of 100. Furthermore, the vacuum envelope, with heavy diffusion pumps hung at odd angles, had numerous low frequency mechanical resonances. Despite these difficulties, we verified the rotational response factor to better than 1%, indicating that atom interferometric rotation sensors perform as predicted. Moreover, we achieved reproducibility at the $42m\Omega_e/\sqrt{sec}$ level. This is about three orders of magnitude more sensitive than previous rotation measurements using atom interferometry[44] and exceeds the sensitivities of much more difficult neutron interferometry measurements that required integration times of many minutes per point[38]. A dedicated rotation sensor using one cm$^2$ gratings and cesium atoms would perform many orders of magnitude better than ours, and should exceed the performance of laser gyroscopes.

**Acknowledgments**

The atom gratings used in this work were made in collaboration with Mike Rooks at the Cornell Nanofabrication Facility at Cornell University[]. We are grateful for the existence and assistance of this facility, and also for help with nanofabrication from Hank Smith and Mark Schattenburg at Massachusetts Institute of Technology. This work was made possible by support from the Army Research Office contracts DAAL03-89-K-0082 and ASSERT 29970-PH-AAS, the Office of Naval Research contract N00014-89-J-1207, National Science Foundation contract 9222768-PHY, and the Joint Services Electronics Program contract DAAL03-89-C-0001,and the Charles Stark Draper Laboratory contract DL-H-484775 9. TDH and ETS acknowledge the support of National Science Foundation graduate fellowships. JS acknowledges the support of an Erwin Schrödinger Fellowship of the Fond zur Förderung der Wissenschaftilchen Forschung in Austria and an APART fellowship of the Austrian Academy of Sciences.

**References**

1. J. Schmiedmayer, M.S. Chapman, C.R. Ekstrom, T.D. Hammond, A. Lenef, R.A. Rubenstein, E.T. Smith, and D.E. Pritchard, "Optics and Interferometry with Atoms and Molecules" to be published in *Atom Interferometry*, ed. P. Berman (Academic Press). The complete review is available via the web at the URL http://coffee.mit.edu/.
2. Troy D. Hammond, "Atom Interferometry: Dispersive Index of Refraction and Rotation Induced Phase Shifts for Matter-Waves," Ph.D. Thesis, M.I.T. February, 1997. Unpublished.
3. J. Schmiedmayer, M.S. Chapman, C.R. Ekstrom, T.D. Hammond, S. Wehinger and D.E. Pritchard, " Phys. Rev. Lett. **74**, 1043 (1995).
4. E. Audouard, P. Duplàa and J. Vigué, Europhys. Lett. **32(5)**, 397 (1995).
5. E. Audouard, P. Duplàa and J. Vigué, "Refractive Index for Atomic Waves: Theory and Detailed Calculations", submitted to: J. de Physique 11 (1995).
6. R.C. Forrey, L. You, V. Kharchenko and A. Dalgarno, "The Index of Refraction of Noble Gases for Sodium Matter Waves", to be published in: Phys. Rev. A (1996).
7. J. Vigué, Phys. Rev. A **52**, 3973 (1995).
8. J.J. Sakurai, *Modern Quantum Mechanics.* (Addison Wesley, Reading, MA, 1985).
9. K.T. Tang and J.P. Toennies, J. of Chem. Phys. **66**, 1496 (1977).
10. K. T. Tang and J.P. Toennies, J. of Chem. Phys. **80**, 3726 (1984).
11. A. H. M. Habets, "Supersonic Expansion of Argon into Vacuum", Ph.D. Thesis, Eindhoven University of Technology (1977). Unpublished.
12. M. J. Rooks, R.C. Tiberio, M.S. Chapman, T.D. Hammond, E.T. Smith, A. Lenef, R.A. Rubenstein, D.E. Pritchard and S. Adams, J. Vac. Sci. Technol. B**13**, 2745 (1995).
13. C. R. Ekstrom, "Experiments with a Separated Beam Atom Interferometer", Ph.D. Thesis, Massachusetts Institute of Technology (1993). Unpublished.
14. P.E. Moskowitz, P.L. Gould, S.R. Atlas and D.E. Pritchard Phys. Rev. Lett. **51**, 370 (1983).
15. P.L. Gould, G.A. Ruff and D.E. Pritchard Phys. Rev. Lett. **56**, 827 (1986).
16. P.L. Gould, G.A. Ruff, P.J. Martin and D.E. Pritchard Phys. Rev. A **36**, 1478 (1987).
17. B.G. Oldaker, P.J. Martin, P.L. Gould, M. Xiao and D.E. Pritchard Phys. Rev. Lett. **65**, 1555 (1990).
18. P.L. Gould, P.J. Martin, G.A. Ruff, R.E. Stoner, J.L. Picque and D.E. Pritchard Phys. Rev. A.**43**, 585 (1991).
19. D.W. Keith, C.R. Ekstrom, Q.A. Turchette and D.E. Pritchard Phys. Rev. Lett. **66**, 2639 (1991).
20. M.S. Chapman, C.R. Ekstrom, T.D. Hammond, J. Schmiedmayer, B. Tannian, S. Wehinger and D.E. Pritchard Phys. Rev. A.**51**, R14 (1995).
21. M.S. Chapman, C.R. Ekstrom, T.D. Hammond, R.A. Rubenstein, J. Schmiedmayer, S. Wehinger and D.E. Pritchard Phys. Rev. Lett. **74**, 4738 (1995).
22. N. Bohr in A. *Einstein: Philosopher - Scientist,* ed. P.A. Schilpp (Library of Living Philosphers, Evanston IL, 1949).
23. R. Feynman, R. Leighton and M. Sands, *The Feynman Lectures on Physics* (Addison-Wesley, Reading MA, 1965).
24. W. Wooters and W. Zurek Phys. Rev. D. **19**, 473 (1979).

25. A. Zeilinger in *New Techniques an Ideas in Quantum Mechanics* (New York Acad. Sci., New York NY, 1986).
26. T. Sleator, O. Carnal, T. Pfau, A. Faulstich, H. Takuma, and J. Mlynek in *Laser Spectroscopy X: Proc. 10th Int. Conf on Laser Spectroscopy,* ed. M. Dulcoy, E. Giacobino, and G. Camy (World Scientific, Singapore, 1991).
27. S.M. Tan and D.F. Walls Phys. Rev. A **47**, 4663 (1993).
28. M.O. Scully, B.-G. Englert, and H. Walther Nature **351**, 111 (1991).
29. E. Schrödinger Naturwissenschaften **23**, 807; ibid. 824; ibid. 844 (1935).
30. M.S. Chapman, T.D. Hammond, A. Lenef, J. Schmiedmayer, R.A. Rubenstein, E.T. Smith and D.E. Pritchard Phys. Rev. Lett.**75**, 3783 (1995).
31. C.J. Bordé Physics Letters A **140**, 10 (1989).
32. P. Storey and C. Cohen-Tannoudji Journal de Physique II **4**, 1999 (1994).
33. T. Pfau, S. Spalter, C. Kurstsiefer, C.R. Ekstrom and J. Mlynek Phys. Rev. Lett. **29**, 1223 (1994).
34. B.G. Englert, H. Fearn, M.O. Scully and H. Walther, "The Micromaser Welcher- Weg Detector Revisited" in *Proceedings of the Adriatico Workshop on Quantum Interferometry,* ed. F. De Martini, G. Denardo, and A. Zeilinger (World Scientific, Singapore, 1994)
35. R. Colella, A.W. Overhauser and S.A. Werner Phys. Rev. Lett. **34**, 1472 (1975).
36. J. Anandan Phys. Rev. D **15**, 1448 (1977).
37. D.M. Greenberger and A.W. Overhauser Rev. Mod. Phys. **51**, 43 (1979).
38. S.A. Werner, J.L. Staudenmann and R. Colella Phys. Rev. Lett. **42**, 1103 (1979).
39. J.F. Clauser Physica B **151**, 262 (1988).
40. A. Lenef, T.D. Hammond, E.T. Smith, M.S. Chapman, R.A. Rubenstein and D.E. Pritchard, Phys. Rev. Lett. January, 1997.
41. M. Kasevich and S. Chu Phys. Rev. Lett. **67**, 181 (1991).
42. D.K. Atwood, M.A. Horne, C.G. Shull and J. Arthur Phys. Rev. Lett. **52**, 1673 (1984).
43. F. Hasselbach, and M. Nicklaus Phys. Rev. A **48**, 143 (1993).
44. F. Riehle, T. Kisters, A. Witte, J. Helmcke and C.J. Bordé Phys. Rev. Lett. **67,** 177 (1991).
45. M. Oberthaler, S. Barnet, E. Rasel, J. Schmiedmayer, and A. Zeilinger submitted to Phys. Rev. A (1996).